

# Constraints from material properties on the dynamics and evolution of Earth's core

Christopher Davies<sup>1,3</sup>, Monica Pozzo<sup>2</sup>, David Gubbins<sup>1,3</sup>, Dario Alfè<sup>2,4</sup>

<sup>1</sup>*School of Earth and Environment, University of Leeds, Leeds LS2 9JT, U.K.*

<sup>2</sup>*Department of Earth Sciences and Thomas Young Centre at UCL, UCL, Gower Street, WC1E 6BT, London, U.K.*

<sup>3</sup>*Institute of Geophysics and Planetary Physics, Scripps Institution of Oceanography, University of California San Diego, 9500 Gilman Drive, La Jolla, CA 92093-0225*

<sup>4</sup>*Department of Physics and Astronomy and London Centre for Nanotechnology, UCL, Gower Street, WC1E 6BT, London, U.K.*

**The Earth's magnetic field is powered from energy supplied by slow cooling and freezing of the liquid iron core. Core thermal history calculations have been hindered in the past by poor knowledge of the properties of iron alloys at the extreme pressures and temperatures pertaining in the core. This obstacle is now being overcome by developments in high pressure experiments and computational mineral physics. Here we review the relevant properties of iron alloys at core conditions and discuss their uncertainty and geophysical implications. Powerful constraints on core evolution are now possible, due partly to recent factor 2–3 upward revision of the all-important electrical and thermal conductivities. This has dramatic implications for the thermal history of the entire Earth, not just the core: the inner core is very young, the core is cooling quickly, and was so hot in the past that the lowermost mantle**

**was almost certainly molten.**

1 Turbulent motions in Earth's liquid outer core, a mixture of iron alloyed with lighter ele-  
2 ments, generate the geomagnetic field through a dynamo process that converts kinetic energy into  
3 magnetic energy. Paleomagnetic observations show that the field has persisted for at least the  
4 last 3.5 billion years<sup>1</sup>, which raises a fundamental question: how was the dynamo powered over  
5 this period? The standard model asserts that mantle convection cools the core by extracting heat  
6 across the core-mantle boundary (CMB); the resulting buoyancy forces drive vigorous convection  
7 that keeps the light element concentration almost uniform and the temperature close to adiabatic.  
8 Cooling leads to freezing of the liquid from the bottom up<sup>2</sup> because the melting curve  $T_m(P)$  in-  
9 creases more rapidly with pressure  $P$  than the adiabat  $T_a(P)$ . As the solid inner core grows, latent  
10 heat is released and the light elements partition selectively into the outer core, reducing its density  
11 compared to pure iron<sup>3</sup> and providing a source of gravitational power<sup>4</sup>. Additional heating comes  
12 from the presence of any radiogenic elements.

13 In general, higher CMB heat flows lead to faster rates of cooling and inner core growth and  
14 provide more power for driving the dynamo (see Methods for mathematical details). Increasing  
15 the conductive heat loss  $Q_a$ , either through a larger thermal conductivity or temperature gradient,  
16 reduces the available power. Since all of the gravitational energy goes into generating magnetic  
17 field it makes the biggest contribution to determining the available dynamo power<sup>5</sup>. As well as the  
18 cooling rate, gravitational energy depends on the nature and molar concentration  $c$  of light elements  
19 and  $\tau = dT_m/dP - \partial T_a/\partial P$ , the difference between adiabatic and melting temperature gradients

20 at the inner core boundary (ICB). Increasing  $c$  enhances the compositional density anomalies while  
21 reducing  $\tau$  means that more inner core material freezes in unit time; for a given cooling rate both  
22 effects act to increase the gravitational energy.

23 Early models of core evolution used ideal solution theory to obtain  $c$  directly from density  
24 without needing to specify the species and represented  $\tau$  in terms of one or more free parameters<sup>6,7</sup>.  
25 The numbers allowed an ancient inner core; the associated gravitational energy powered the geo-  
26 dynamo over most of Earth's history, negating any concerns over sustaining a dynamo powered  
27 by thermal convection alone. This scenario became untenable following an upward revision of  
28  $T_a$ , which increased the adiabatic gradient and hence the heat  $Q_a$  conducted down the adiabat (see  
29 equations (1) and (2) below). The prevailing view was that the inner core must be a young feature  
30 of the planet, around 1 billion years old<sup>8</sup>, and that thermal convection alone could power the dy-  
31 namo prior to inner core formation<sup>9</sup>. However, thermal history models still produced a wide range  
32 of results, owing to different choices for material properties rather than theoretical formulations<sup>9</sup>.

33 The technical challenge of estimating core properties arises from the extreme pressures  
34 (135 – 330 GPa) and temperatures ( $\sim 5000$  K). This challenge is now being met by *ab initio*  
35 calculations and by diamond anvil cell and shock wave experiments where available. *Ab initio*  
36 calculations deliver all the geophysically relevant parameters at the full range of core ( $P, c, T$ )  
37 conditions; they are ground truthed from experiments, which are usually conducted in more re-  
38 strictive ( $P, c, T$ ) regimes. Diamond anvil cell experiments are normally only available to upper  
39 core ( $P, T$ ) conditions, while shock wave experiments follow an equation of state defined by the

40 physical properties of the material (the Hugoniot), and are therefore not able to explore the full  
41  $(P, T)$  space relevant to the core (pre-heating or pre-compressing allows to move somewhat in  
42  $(P, T)$  space, but still not enough to cover all the relevant conditions). Examples of validations  
43 of *ab initio* calculations on pure iron include the equation of state of the hexagonal close-packed  
44 crystal up to core pressures, both at room temperature<sup>10–14</sup> and on the Hugoniot<sup>15,16</sup>, the speed  
45 of sound of the liquid<sup>16,17</sup>, the isentropic compressibility and thermal expansivity of the solid on  
46 the Hugoniot<sup>15,16</sup>, the phonon dispersions (vibrational frequencies of waves in crystals as func-  
47 tion of wave-vector) of the body centered cubic crystal at ambient conditions<sup>14,18</sup>, the density of  
48 states of hexagonal close-packed iron up to 150 GPa<sup>19</sup>, the iron melting curve<sup>17,20</sup>, and the ambient  
49 conditions electrical resistivity<sup>21,22</sup>.

50       The most difficult quantities to calculate at core conditions happen to be the most critical  
51 for core and geodynamo models: thermal and electrical conductivities. Results have only been  
52 obtained recently<sup>23–28</sup>, and turn out to be 2–3 times higher than conventional estimates<sup>29,30</sup> (called  
53 “low” conductivities below) of  $k = 28 - 46 \text{ W m}^{-1} \text{ K}^{-1}$ . Crucially these new values (called  
54 “high” conductivities below) have been obtained in both experiments and *ab initio* calculations. A  
55 very recent study<sup>31</sup> on a perfect iron crystal at ICB conditions suggests that a new effect (electron-  
56 electron scattering) would reduce the electrical conductivity back to old values that were estimated  
57 for the liquid<sup>29</sup>. The proposed importance of strong correlation effects appears at odds with previ-  
58 ous work<sup>32</sup>, and so these results await both experimental and theoretical confirmation. Because of  
59 this we mainly focus on the high conductivity values, although the lower values are included for  
60 completeness.

61 Here we present a synthesis of core material properties. Parameter values are discussed,  
62 followed by their geophysical significance. A brief description of the *ab initio* methods is provided  
63 in the Methods.

## 64 **1 Material Properties for Earth's Core**

65 The thermodynamic state of the core is determined by 3 intensive variables: Pressure  $P$ , molar  
66 concentration  $c_X$  of species  $X$ , and temperature  $T$ . Pressure is very close to the enormous hy-  
67 drostatic pressure, which is accurately determined from seismology by integrating  $dP/dr = -\rho g$   
68 over radius  $r$ . Here  $\rho$  is density and  $g$  is gravity. Constraints on  $c_X$  and  $T$  are derived from the  
69 seismically-determined ICB density jump,  $\Delta\rho$ .

70 Part of the observed density jump<sup>17</sup>,  $\Delta\rho_m = 0.24 \text{ gm cc}^{-1}$  is due to the phase change at the  
71 ICB; the rest determines the excess concentration of light element in the outer core, which in turn  
72 affects the core temperature and influences almost all terms in the energy and entropy budgets.  
73 Normal mode eigenfrequencies give a consistent result of  $\Delta\rho = 0.8 \pm 0.2 \text{ gm cc}^{-1}$  but have low  
74 resolution of about  $400 \text{ km}^3$ . Body waves have much better resolution of a few kilometers, but  
75 the estimates vary widely because PKiKP is a noisy phase<sup>34-36</sup>; an upper bound of  $1.1 \text{ gm cc}^{-1}$   
76 has been estimated<sup>36</sup>. There is also evidence for an anomalously dense layer in the lowermost  
77  $150 \text{ km}$  of the outer core<sup>37</sup>, which probably has a chemical origin<sup>38</sup>. Two explanations have been  
78 proposed: the layer could be a stable density-stratified zone of partial melt through which light  
79 elements pass by progressive melting and freezing<sup>38</sup>, or parts of the inner core could be melting,

80 releasing excess heavy liquid into the outer core<sup>39</sup>. In either case normal modes would measure the  
81 density difference between the inner core and main part of the outer core while body waves would  
82 measure the smaller difference between the solid inner core and the heavy liquid in the anomalous  
83 layer. We believe the normal mode estimates are more likely to represent the true compositional  
84 difference between the outer and inner cores. We consider 3 values  $\Delta\rho = 0.6, 0.8$  and  $1.0 \text{ gm cc}^{-1}$   
85 spanning the range of published estimates. The 0.6 value corresponds to PREM<sup>40</sup>.

86 Table 1 summarises our best estimates of core material properties for pure iron and the 3  
87 values of  $\Delta\rho$ . Supplementary Table 1 is an extended version of Table 1 and Supplementary Tables  
88 2–4 provide polynomial representations of depth-varying properties. Models are labeled by the  
89 corresponding core composition as described below. After discussing composition, the thermal  
90 properties for each model are described followed by transport properties, which must be calculated  
91 for a given composition at specific  $(P, T)$  conditions.

92 **Composition** is determined from the density (see Methods) and seismic velocities by comparing  
93 them with calculated values for mixtures of iron and candidate siderophile elements: Si and O  
94 because of their abundance and S because of its presence in iron meteorites, which are thought to  
95 be remnants of planetary cores. Other elements, e.g. H, have been proposed<sup>41</sup> but their properties  
96 in iron mixtures have not yet been explored extensively. The core also probably contains some Ni;  
97 however, recent experiments found that adding up to 10% of Ni does not change the hexagonal  
98 close-packed crystal structure of the solid<sup>42</sup>, while *ab initio* calculations suggest that at high  $T$  the  
99 seismic properties of Fe-Ni alloys are almost indistinguishable from those of pure iron<sup>43</sup>. Recent

100 studies of core composition<sup>44–46</sup> conclude that the light elements are likely to be Si, S, and O with  
101 negligible amounts of H and C. *Ab initio* calculations for binary mixtures of Si, S, and O with Fe  
102 show that S and Si partition almost equally between solid and liquid, while almost all the O goes  
103 into the liquid<sup>14,45</sup>. The behaviour of S and Si are very similar<sup>14</sup> so we use a Fe-Si-O mixture in  
104 this review. Molar concentrations of species  $X$  for the solid and liquid,  $c_X^s$  and  $c_X^l$  respectively, are  
105 given in section 1 of Table 1; each model is named after the corresponding mass concentration.

106 **Temperature.** Light element  $X$  depresses the melting temperature for pure iron,  $T_m$ , by an amount  
107  $\Delta T_X$ . Of particular importance are conditions near the ICB (radius  $r = r_i$ ,  $P = 330$  GPa). The  
108 large volume of work on  $T_m$  is summarised elsewhere<sup>20,47</sup>. Some studies have shown encourag-  
109 ing agreement, with  $T_m(r_i) = 6350 \pm 300$  K predicted by diamond anvil cell experiments up  
110 to 82 GPa<sup>47</sup> and 200 GPa<sup>20</sup>, shock experiments at 225–260 GPa<sup>48</sup> and *ab initio* calculations at  
111 330 GPa<sup>14,49</sup>. This value is used in Section 2 of Table 1. Other calculations<sup>50,51</sup> have found  
112  $T_m(r_i) = 7100$  K and  $T_m(r_i) = 5400$  K respectively, but these only used *ab initio* indirectly by  
113 fitting an interatomic potential which has different melting properties from those of the fully *ab*  
114 *initio* system<sup>52</sup>.

115 Along with  $T_m$  and the core chemistry model, the entropy of melting for pure iron  $\Delta S$  is  
116 needed to determine  $\Delta T_X$  at the ICB<sup>49</sup>. The core temperature at the ICB,  $T_i$ , equals the melting  
117 temperature of the mixture; the values in section 3 of Table 1 are calculated from  $T_i = T_m + \Delta T_m =$   
118  $T_m + \Delta T_O + \Delta T_{Si}$ . The latent heat  $L$  released on freezing the inner core is  $L = T_m \Delta S$  (section 2  
119 of Table 1).

120 In regions where convection is active the outer core temperature follows an adiabat, given by

$$T_a = T_i \exp \left( - \int_{r_i}^r \frac{\rho g \gamma}{K_s} dr \right), \quad (1)$$

121 where  $\gamma$  is the thermodynamic Grüneisen parameter. Note that  $\partial T_a / \partial r = -\rho g \gamma T_a / K_s$ . The bulk  
 122 modulus,  $K_s$ , and gravity,  $g$ , are calculated directly in *ab initio* methods and are very similar to  
 123 PREM. *Ab initio* calculations have found that  $\gamma \approx 1.5$  at the CMB and remains constant<sup>17</sup> (to with  
 124 the accuracy of the calculations) or decreases slightly<sup>53,54</sup> with depth. The depth variation reduces  
 125 the adiabatic gradient at the ICB, and hence  $\tau = dT_m/dP - \partial T_a/\partial P$ , but makes little difference  
 126 to  $T_a$ . Depth variation of  $T_a$  is therefore well-constrained. The three adiabats used in our core  
 127 evolution calculations (section 2) are shown in Figure 1; values for the CMB and ICB gradients  
 128 are given in section 3 of Table 1. In the inner core,  $T_a$  was assumed to be close to isothermal<sup>27</sup>.

129 The thermal and chemical expansion coefficients,  $\alpha_T = \rho^{-1}(\partial \rho / \partial T)_{P,c}$  and  
 130  $\alpha_c = -\rho^{-1}(\partial \rho / \partial c)_{P,T}$  respectively, determine the buoyancy forces arising from thermal and  
 131 compositional anomalies.  $\alpha_T$  can be obtained from a number of thermodynamic relations, e.g.  
 132  $\alpha_T = \gamma \rho C_p / K_s$ . *Ab initio* calculations have found the specific heat  $C_p = 700 - 800 \text{ J kg}^{-1} \text{ K}^{-1}$   
 133 independent of radius<sup>54,55</sup>, in agreement with theory<sup>56</sup> and hence  $\alpha_T$  is a decreasing function of  
 134 depth<sup>55,56</sup> because of the factor  $\rho / K_s$ . The compositional expansion coefficient  $\alpha_c$  is different for  
 135 each element; values obtained at the present ICB ( $P, T$ ) conditions<sup>49</sup> are given in Table 1.

136 **Transport Properties.** The geophysical importance of core thermal ( $k$ ) and electrical ( $\sigma$ ) con-  
 137 ductivities is discussed below.  $\sigma$  is easier to obtain and is sometimes used to infer  $k$  through the  
 138 Wiedemann-Franz law, although there are situations when this relation does not hold (see Meth-



139 ods). Recent estimates of  $k$  and  $\sigma$  for pure iron<sup>23,24</sup> are 3–5 times higher at the CMB than pre-  
140 vious estimates<sup>29,30</sup> and increase by a factor of 1.5 to the ICB. Mixtures have also been studied,  
141 though using different compositions and adiabats. Despite this, and the different methods used,  
142 the different studies all find  $k$  at the CMB in the range 80–110 W m<sup>-1</sup> K<sup>-1</sup>, increasing up to 140–  
143 160 W m<sup>-1</sup> K<sup>-1</sup> at the ICB<sup>23,25,26</sup> (Figure 1). There is a jump in both  $k$  and  $\sigma$  at the ICB and a  
144 small increase across the inner core<sup>27</sup>.

145 Mass diffusion coefficients  $D_X$  relate the concentration gradient of species  $X$  to the diffusive  
146 flux of that species. Recent estimates<sup>25,57</sup> of  $D_O$  and  $D_{Si}$  for O and Si are in line with previous  
147 calculations at CMB pressures<sup>58</sup>; and show a factor 1.5 increase to the ICB. In core evolution mod-  
148 els  $D_X$  enters the barodiffusion term, which describes the entropy generated by diffusion of light  
149 elements down the ambient pressure gradient. The effect is measured by the barodiffusive coeffi-  
150 cients  $\alpha_X^D$ , which are calculated using the values of  $D_X$  and  $(\partial\mu/\partial c_X)_{P,T}$  in Table 1, where  $\mu$  is the  
151 chemical potential<sup>58</sup>. Barodiffusion is small enough to be neglected in the entropy budget<sup>9,58,59</sup>,  
152 but might play a dynamical role near the top of the core (see the “stratification” subsection below).

153 The kinematic viscosity  $\nu$  plays a key role in the dynamics of rotating fluids<sup>60</sup>, but is less  
154 important for determining long-term core evolution. Recent *ab initio* estimates<sup>25,57</sup> of  $\nu$  are pre-  
155 sented in Table 1 using the core chemistry model adopted in this review; they are in line with older  
156 values<sup>61</sup>.

## 157 2 Geophysical Implications of Revised Core Properties

158 **Core Energy Budget.** The dynamo entropy  $E_J$  represents the work done by buoyancy forces that  
159 goes into generating magnetic field<sup>5</sup> and is therefore crucial for assessing the viability of dynamo  
160 action. Both  $E_J$  and the CMB heat flow  $Q_{\text{cmb}}$  are related to the core cooling rate through the  
161 material properties described above: higher heat flow yields faster cooling and higher  $E_J$  (see  
162 Methods for technical details). The cooling rate determines the inner core age. Mantle convection  
163 sets the CMB heat flow and various lines of evidence suggest  $Q_{\text{cmb}} = 5 - 15$  TW at present<sup>62,63</sup>.  
164  $E_J$  could be calculated directly if we had detailed knowledge of the magnetic field throughout the  
165 core; however the main field contributions to  $E_J$  occur at scales that cannot be observed<sup>64</sup> and so  
166  $E_J$  is determined from  $Q_{\text{cmb}}$  for the present-day. On longer timescales, where both  $Q_{\text{cmb}}$  and  $E_J$   
167 are hard to estimate, the constraint  $E_J \geq 0$  can be used to calculate lower bounds on the cooling  
168 rate. All parameters values are given in Table 1; where there is a range the number highlighted in  
169 red has been used in the calculation.

170 Increasing  $\Delta\rho$  increases the outer core light element concentration and reduces the adiabatic  
171 gradient (because  $\partial T_a/\partial r$  is proportional to  $T_a$ ), allowing the same  $E_J$  to be balanced with a lower  
172 cooling rate and hence lower  $Q_{\text{cmb}}$  (Figure 2). For a plausible value<sup>65</sup> of  $E_J = 400$  MW K<sup>-1</sup>,  
173 increasing  $\Delta\rho$  from 0.6 to 1.0 gm cc<sup>-1</sup> reduces the required CMB heat flow by  $\approx 2$  TW with low  
174 conductivity and  $\approx 2$  TW with high conductivity.

175 Increasing  $k$  increases the amount of heat conducted away down the adiabatic gradient, and  
176 hence reduces the dynamo efficiency (Figure 2). The stability of core convection also depends

177 critically on  $k$ . The total adiabatic heat flow is

$$Q_a = 4\pi k(r_o)r_o^2 \left. \frac{\partial T_a}{\partial r} \right|_{r=r_o}, \quad (2)$$

178 where  $r_o = 3480$  km is the CMB radius. When  $Q_{\text{cmb}} > Q_a$  the whole core is superadiabatic and  
179 thermal convection occurs everywhere; when  $Q_{\text{cmb}} < Q_a$  the top of the core is subadiabatic and  
180 stable to thermal convection. For a low value of  $k = 28$  W m<sup>-1</sup> K<sup>-1</sup> the core is thermally unstable  
181 ( $Q_{\text{cmb}} > Q_a$ ) and generates a magnetic field ( $E_J \geq 0$ ) for all estimates of present-day CMB heat  
182 flow (Figure 2). For the high values of  $k$  dynamo action requires a minimum of 5.5–7.5 TW, while  
183 the top of the core is likely to be thermally stable unless  $Q_{\text{cmb}} \approx 15$  TW which is very high, around  
184 one third of the total heat leaving Earth’s surface<sup>66</sup>. Maintaining  $E_J = 400$  MW K<sup>-1</sup> with the new  
185  $k$  values requires 9–13 TW with composition driving convection against thermal stratification in  
186 the uppermost core (Figure 2).

187 **Thermal History.** To evidence the effect of material properties on predictions of past core evolu-  
188 tion we set  $E_J = 0$  prior to inner core formation and then specify  $Q_{\text{cmb}}$  during inner core growth.  
189 This prescription<sup>9,59,63</sup> ensures that  $Q_{\text{cmb}}$  always exceeds the conducted heat, consistent with the  
190 modeling assumptions (see Methods), and produces conservative estimates of the cooling rate,  
191 core temperature and inner core age. Figure 3 shows predicted inner core age and CMB tem-  
192 perature ( $T^{3.5\text{Ga}}$ ) and CMB heat flow ( $Q^{3.5\text{Ga}}$ ) at 3.5 Ga, the time of the earliest paleomagnetic  
193 measurement<sup>1</sup>. Models span the range  $\Delta\rho = 0.6 - 1.0$  gm cc<sup>-1</sup> and the range of  $k$  (Figure 1). We  
194 also show the effect of adding 300 ppm <sup>40</sup>K at the present day, which likely represents an extreme  
195 scenario<sup>44,63</sup>. The shaded temperature range of  $4150 \pm 150$  K corresponds to present estimates  
196 of the lower mantle solidus temperature<sup>67</sup>; core temperatures exceeding this range suggest partial

197 melting in past.

198 Low  $k$  values predict inner core ages of  $\sim 1$  Ga or more, CMB heat flows below 10 TW  
199 over the last 3.5 Ga and ancient core temperatures at or above the lower mantle solidus estimates.  
200 With the high  $k$  values there is little doubt that the lowermost mantle would have been partially  
201 molten in the past. Moreover, the high  $k$  models consistently yield inner core ages of  $\sim 0.6$  Ga or  
202 younger. Radiogenic heating does little to change the results. Figure 3 also shows favoured models  
203 from four recent studies<sup>63,68–70</sup> that used the high  $k$  values and imposed different constraints on the  
204 time-variation of  $E_J$ . A consistent picture emerges in which 1) the inner core is at most 500–700  
205 million years old; 2) ancient core temperatures greatly exceeded present estimates of the lower  
206 mantle solidus; 3) high ancient CMB heat flows were needed to power the early geodynamo.

207 Increasing  $\Delta\rho$  from  $0.6 \text{ gm cc}^{-1}$  to  $1.0 \text{ gm cc}^{-1}$  can produce a 400–600 K decrease in  $T^{3.5\text{Ga}}$   
208 and a 200–400 Myr increase in the inner core age depending on the details on the model (Figure 3).  
209 Figure 4 shows how the results from a single reference case in Figure 3 are influenced by vary-  
210 ing values for several material properties compared to the numbers in Table 1. Where errors are  
211 not reported a  $\pm 10\%$  variation is assumed, which is likely to be larger than errors in the *ab initio*  
212 calculations<sup>17,55</sup>. Individually changing  $\alpha_c$  or  $L$  by  $\pm 10\%$ ,  $C_p$  to the values of a previous study<sup>56</sup>,  
213 core density from PREM to AK135<sup>71</sup>, or the melting curve to a recent experimental profile<sup>20</sup> (de-  
214 noted  $T_m^A$ ) each make little difference. Using a depth-variable  $\gamma$  (denoted  $\gamma^J$ )<sup>54</sup> makes a small  
215 change to the inner core age but barely changes  $T^{3.5\text{Ga}}$ . The biggest changes arise from varying  
216  $k$  and allowing for the  $\pm 300$  K uncertainty in  $T_i$ . Combining the variations to give the youngest

217 (oldest) inner core yields changes of  $\pm 400$  K in  $T^{3.5\text{Ga}}$  and  $\pm 150$  Myrs in inner core age  
218 compared to the reference model, which is a comparable effect to uncertainty in  $\Delta\rho$  alone.

219 **Stratification Beneath the CMB.** Observed variations in the magnetic field only reflect changes  
220 at the top of the core and so the dynamic stability of this region is an important issue. Stratified lay-  
221 ers are dynamically very different to convecting regions: they suppress radial motion and support  
222 a different suite of wave motions<sup>72</sup>. In the absence of chemical or boundary effects, subadiabatic  
223 conditions at the top of the core (Figure 2) should result in stable stratification. Compositional  
224 convection could overcome this stratification and mix the excess heat downwards, restoring adia-  
225 batic conditions everywhere<sup>73</sup>. Alternatively, light elements could enhance thermal stratification if  
226 they are emplaced at the top of the core early in Earth's history<sup>74</sup> or pool beneath the CMB over  
227 time. Pooling could arise from light element transfer across the CMB<sup>75</sup>, by barodiffusion of light  
228 elements up the ambient pressure gradient<sup>76</sup>, or by the transfer of chemically distinct blobs from  
229 the ICB<sup>74,77</sup>.

230 Pooling mechanisms produce layers of  $\sim 100$  km depth<sup>75,76</sup>, comparable to values inferred  
231 from geomagnetism<sup>78</sup>, but thinner than recent seismic estimates<sup>79</sup>. Whether compositional con-  
232 vection can overcome thermal stratification requires detailed analyses of the different buoyancy  
233 sources<sup>26,80,81</sup>. Two recent studies<sup>78,81</sup> find a thermochemically stable layer of  $\sim 100$  km for a  
234 CMB heat flow of  $\approx 13\text{TW}$ , in the range of current estimates<sup>62</sup>. Estimates of the associated den-  
235 sity gradients from the recently-proposed thermal/chemical stable layers yield Brunt frequencies  
236 of  $O(1)$  day<sup>75,76,81</sup>, eliminating any long-period vertical motion.

237 Density anomalies associated with core motions are so small that convection is unlikely to  
238 entrain or penetrate a stable layer<sup>26,72,75,76</sup>. The effect on a stable layer of thermal anomalies in the  
239 lowermost mantle is not so clear. The large-scale pattern of CMB heat flow can be constructed by  
240 assuming that observed seismic velocity variations represent thermal heterogeneity. The strength  
241 of the lateral variations is measured by the parameter  $q^* = (q^{\max} - q^{\min}) / (q_{\text{cmb}} - q_a)$ , the ratio  
242 of peak-to-peak boundary heat flow variations to the mean superadiabatic heat flow per unit area.  
243 Mantle convection simulations<sup>82</sup> have estimated  $q^* \approx 2$ , but did not appear to subtract the adiabat.  
244 In any case, the new values of  $k$  increase  $q_a$  and hence  $q^*$ , further strengthening the effect.

245 Geodynamo simulations with  $q^* \approx 1$  produce flows with persistent downwellings below  
246 regions of high CMB heat flow that concentrate magnetic flux there, producing field morpholo-  
247 gies that are similar to the historical geomagnetic field<sup>83,84</sup>. These effects will be amplified when  
248 convection is weak at the top. Boundary-driven radial motions may generate flow in a stratified  
249 layer<sup>81</sup>, as has been observed in non-magnetic simulations with weak stratification<sup>85</sup>. Geodynamo  
250 simulations that combine strong stratification and strong boundary forcing ( $q^* \gg 1$ ) are needed to  
251 establish the dynamics that win out.

252 The depth increase of  $k$  opens up the possibility that the very top of the core is superadiabatic,  
253 with a stable layer directly below<sup>26,80</sup>. The conditions required to form such a layer are sensitive  
254 to the  $k(r)$  profile; the adiabats and corresponding  $k(r)$  profiles used in this review do not produce  
255 the effect.

256 **Magnetic timescales.** Revised core viscosity and diffusivities (Table 1) are still too small to be  
257 used in present geodynamo simulations. This situation is unlikely to change in the next ten years<sup>60</sup>.  
258 However, changes to the electrical conductivity  $\sigma$  are significant. The new (high) values of  $\sigma$  give  
259 a magnetic diffusivity of  $\eta = 0.7 \text{ m}^2 \text{ s}^{-1}$  at the CMB and  $\eta = 0.6 \text{ m}^2 \text{ s}^{-1}$  at the ICB compared to  
260  $\eta = 1.6 \text{ m}^2 \text{ s}^{-1}$  using an old (low) value<sup>29</sup> of  $\sigma = 5 \times 10^5 \text{ S m}^{-1}$ . Lowering  $\eta$  raises the Magnetic  
261 Reynold's number  $Rm = Ur_o/\eta$  from  $\approx 700$  to  $\approx 1500$ , where  $U$  is the root mean square velocity  
262 at the top of the core<sup>25,26</sup>.  $Rm$  must be sufficiently large to generate a magnetic field by dynamo  
263 action. Decreasing  $\eta$  makes dynamo action possible with slower flows.

264 The time for a dipole magnetic field (the slowest decaying mode) to decay in a uniform  
265 sphere of radius  $r_o$ , the dipole decay time  $\tau_d = r_o^2/\pi^2\eta$ , is increased from 25 kyrs to 55 kyrs with  
266 the revised  $\sigma$  values. This result changes interpretations of all geomagnetic observations in terms of  
267 diffusion processes. In particular, polarity reversals of the field, which take 1–10 kyrs to complete,  
268 now appear fast on the diffusion timescale.  $\tau_d = 10 \text{ kyr}$  for the inner core, comparable to the  
269 timescale of reversal transition. Whether this is coincidence or a characteristic that distinguishes  
270 reversals from excursions<sup>86</sup> (where the new polarity is not retained) remains to be tested with  
271 modern geodynamo models.

272 **Inner Core Convection.** Seismic observations have revealed surprising structural complexity in  
273 the inner core, including hemispherical and radial variations in velocity and anisotropy<sup>37</sup>. Much re-  
274 cent work has focused on explaining these observations by solid-state convection<sup>87</sup>. Thermal con-  
275 vection requires the inner core to be superadiabatic; with the high values of  $k \sim 200 \text{ W m}^{-1} \text{ K}^{-1}$

276 (Figure 1) this requires  $Q_{\text{cmb}} = 30 - 60$  TW at the present-day<sup>27,70,88</sup>, at least two thirds of the  
277 surface heat flow<sup>66</sup>. Just after inner core nucleation, 500-700 Myr ago (Figure 3), an estimated  
278 30 TW is needed<sup>27</sup>. Mantle heat sources are unlikely to have changed significantly in this period<sup>89</sup>;  
279 30 TW probably represents at least half of Earth's total heat budget at this time.

280 Inner core convection could be driven compositionally if less light element partitions into it  
281 over time. Compositionally unstable conditions may have arisen once the inner core grew beyond  
282  $O(10)$  km, but probably have not persisted to the present day<sup>59,70</sup>. The case of thermochemical  
283 buoyancy is complicated by possible double-diffusive effects; initial studies indicate that the net  
284 buoyancy force is stabilising<sup>90</sup>. Overall it seems that inner core convection, either in the plume<sup>87</sup> or  
285 translation<sup>39,91</sup> regimes, is unlikely at present. This is consistent with a recent review that favours  
286 texturing mechanisms arising from magnetic coupling or heterogeneous growth due to enhanced  
287 equatorial heat loss<sup>88</sup>. If heterogeneous ICB heat flow is related to recent geomagnetic phenomena  
288 such as weak secular variation in the Pacific hemisphere<sup>92</sup> or long-term tilt of the dipole axis<sup>93</sup> then  
289 another mechanism (aside from convection) may be needed to explain the origin of the forcing.

### 290 **3 Core Dynamics and Evolution with High Conductivities**

291 The material properties of liquid iron alloys at high pressures and temperatures are now suffi-  
292 ciently well-known to draw robust conclusions about the long-term evolution of the core. Recent  
293 calculations with the new (high) conductivities find that 1) The inner core age is less than 500-  
294 700 Ma<sup>24,59,63,80</sup>; 2) high early CMB heat flow and corresponding core temperatures that signifi-



295 cantly exceeded present estimates of the lower mantle solidus temperature<sup>59,63,68,94</sup> imply partial  
296 melting of the lowermost mantle in the past; 3) the present-day core is subadiabatic at the top and  
297 may be stably stratified<sup>24,26,80</sup>. Prior to the new conductivity estimates, models predicted inner core  
298 nucleation 1 billion years ago<sup>8</sup>, early core temperatures comparable to the lower mantle solidus<sup>9</sup>,  
299 and superadiabatic conditions throughout the core at the present-day.

300 In terms of geophysical significance the most uncertain properties are the iron melting curve  
301  $T_m$  and the ICB density jump  $\Delta\rho$ . However, the preceding conclusions will hold unless  $\Delta\rho$  or  $T_m$   
302 have been drastically underestimated. Core composition is also important: we have used an Fe-  
303 Si-O model, but other species such as H and C have been proposed. The effects of other putative  
304 light elements can now be investigated routinely using *ab initio* methods and the results evaluated  
305 against geophysical constraints. The viability of a given composition is no longer a matter for  
306 speculation. Finally, there is still some debate over the conductivity. The implications of old (low)  
307 conductivity values are shown in Figures 2 and 3. We favour the high values and discuss the their  
308 implications below.

309 Revised core evolution models indicate that powering the dynamo around 3.5 Ga required a  
310 minimum  $Q_{\text{cmb}} \approx 15 - 25$  TW to be extracted from the core by a partially molten lower mantle.  
311 The actual required  $Q_{\text{cmb}}$  at this time was likely much greater. Internal heat production within a  
312 magma ocean due to latent heat release and/or radiogenic sources will insulate the core, further  
313 exacerbating the heat problem<sup>95</sup>. It has been proposed that the insulating effect was so drastic as to  
314 delay the onset of the core dynamo until  $\sim 2$  Ga, with the magma ocean generating the field before

315 this time<sup>96</sup>. Whether cooling alone is sufficient to power the early dynamo is currently an open  
316 question; indeed, the search for alternative energy sources has already begun<sup>97</sup>.

317 At present the uppermost core is subadiabatic unless  $Q_{\text{cmb}}$  has been underestimated; how-  
318 ever, this seems unlikely based on the power requirements for mantle convection<sup>62</sup>. The magnetic  
319 field is then generated by vigorous convection deep within the core, powered by latent heat release  
320 and gravitational energy. If light elements pool at the CMB the top of the core will be stably strat-  
321 ified. Lateral variations in CMB heat flow are superimposed on the stratified layer. Geomagnetic  
322 data are presently unable to unambiguously identify a stable layer<sup>98,99</sup>, although a recent constraint  
323 on core electrical conductivity from long-term dipole field variations is consistent with the high  
324 conductivity estimates that argue in favour of stratification<sup>100</sup>. In isolation both a stable layer and  
325 lateral heat flow variations can explain prominent features of the present geomagnetic field: wave  
326 motions in a  $\sim 100$  km-thick stable layer can account for short-period fluctuations in the dipole  
327 field<sup>78</sup>; regions of high CMB heat flow can concentrate magnetic field lines, producing the four  
328 dominant high-latitude flux patches<sup>83</sup>; low heat flow beneath the Pacific can explain the weak  
329 secular variation there<sup>85</sup>. Progress towards a coherent dynamical model of the present-day core re-  
330 quires 1) a coherent seismological picture of core stratification; 2) explaining recent geomagnetic  
331 secular variation in terms of stable layer dynamics and; 3) analysis of the interaction between a  
332 stable region CMB heat flow variations. The origin of a stable layer poses yet more fascinating  
333 challenges for future research.

334

- 335 1. Tarduno, J. *et al.* Geodynamo, solar wind, and magnetopause 3.4 to 3.45 billion years ago.  
336 *Science* **327**, 1238–1240 (2010).
- 337 2. Jacobs, J. The Earth's inner core. *Nature* **172**, 297–300 (1953).
- 338 3. Birch, F. Elasticity and the constitution of Earth's interior. *J. Geophys. Res.* **66**, 227–286  
339 (1952).
- 340 4. Braginsky, S. Structure of the F layer and reasons for convection in the Earth's core. *Sov.*  
341 *Phys. Dokl.* **149**, 8–10 (1963).
- 342 5. Lister, J. & Buffett, B. The strength and efficiency of thermal and compositional convection  
343 in the geodynamo. *Phys. Earth Planet. Int.* **91**, 17–30 (1995).
- 344 6. Stevenson, D., Spohn, T. & Schubert, G. Magnetism and thermal evolution of the terrestrial  
345 planets. *Icarus* **54**, 466–489 (1983).
- 346 7. Mollett, S. Thermal and magnetic constraints on the cooling of the Earth. *Geophys. J. R.*  
347 *Astr. Soc.* **76**, 653–666 (1984).
- 348 8. Labrosse, S., Poirier, J.-P. & Le Moëul, J.-L. The age of the inner core. *Earth Planet. Sci.*  
349 *Lett.* **190**, 111–123 (2001).
- 350 9. Nimmo, F. Thermal and compositional evolution of the core. In Schubert, G. (ed.) *Treatise*  
351 *on Geophysics, Vol. 9*, 217–241 (Elsevier, Amsterdam, 2007).
- 352 10. Söderlind, P., Moriarty, J. A. & Wills, J. M. First-principles theory of iron up to Earth-core  
353 pressures: Structural, vibrational, and elastic properties. *Phys. Rev. B* **53**, 14063 (1996).

- 354 11. Vočadlo, L., de Wijs, G. A., Kresse, G., Gillan, M. & Price, G. D. First principles calculations  
355 on crystalline and liquid iron at Earth's core conditions. *Faraday Discuss.* **106**, 205 (1997).
- 356 12. Mao, K., Wu, Y., Chen, L. C., Shu, J. F. & Jephcoat, A. P. Static compression of iron to  
357 300 GPa and Fe<sub>0.8</sub>Ni<sub>0.2</sub> alloy to 260 GPa: implications for the composition of the core. *J.*  
358 *Geophys. Res.* **95**, 21737 (1990).
- 359 13. Dewaele, A. *et al.* Quasihydrostatic equation of state of iron above 2 Mbar. *Phys. Rev. Lett.*  
360 **97**, 215504 (2006).
- 361 14. Alfè, D., Gillan, M. J. & Price, G. D. Temperature and composition of the Earth's core.  
362 *Contemp. Phys.* **48**, 63–80 (2007).
- 363 15. Alfè, D., Price, G. & Gillan, M. Thermodynamics of hexagonal close packed iron under  
364 Earth's core conditions. *Phys. Rev. B* **64**, 045123 (2001).
- 365 16. Brown, J. M. & McQueen, R. G. Phase transitions, Grüneisen parameter, and elasticity for  
366 shocked iron between 77 GPa and 400 GPa. *J. Geophys. Res.* **91**, 7485 (1986).
- 367 17. Alfè, D., Price, G. & Gillan, M. Iron under Earth's core conditions: Liquid-state thermody-  
368 namics and high-pressure melting curve from *ab initio* calculations. *Phys. Rev. B* **65**, 165118  
369 (2002).
- 370 18. Brockhouse, B. N., Abou-Helal, H. E. & Hallman, E. D. Lattice vibrations in iron at 296 K.  
371 *Solid State Commun.* **5**, 211 (1967).
- 372 19. Mao, H. K. *et al.* Phonon density of states of iron up to 153 GPa. *Science* **292**, 914 (2001).

- 373 20. Anzellini, S., Dewaele, A., Mezouar, M., Loubeyre, P. & Morard, G. Melting of iron at  
374 Earth's inner core boundary based on fast x-ray diffraction. *Science* **340**, 464–466 (2013).
- 375 21. Alfè, D., Pozzo, M. & Desjarlais, M. Lattice electrical resistivity of magnetic bcc iron from  
376 first-principles calculations. *Phys. Rev. B* **85**, 1–5 (2012).
- 377 22. Weiss, R. J. & Marotta, A. S. Spin-dependence of the resistivity of magnetic metals. *J. Phys.*  
378 *Chem. Solids* **9**, 302–308 (1959).
- 379 23. de Koker, N., Steinle-Neumann, G. & Vojtech, V. Electrical resistivity and thermal conduc-  
380 tivity of liquid Fe alloys at high P and T and heat flux in Earth's core. *Proc. Natl. Acad. Sci.*  
381 **109**, 4070–4073 (2012).
- 382 24. Pozzo, M., Davies, C., Gubbins, D. & Alfè, D. Thermal and electrical conductivity of iron at  
383 Earth's core conditions. *Nature* **485**, 355–358 (2012).
- 384 25. Pozzo, M., Davies, C., Gubbins, D. & Alfè, D. Transport properties for liquid silicon-oxygen-  
385 iron mixtures at Earth's core conditions. *Phys. Rev. B* **87**, 014110 (2013).
- 386 26. Gomi, H. *et al.* The high conductivity of iron and thermal evolution of the Earth's core. *Phys.*  
387 *Earth Planet. Int.* **224**, 88–103 (2013).
- 388 27. Pozzo, M., Davies, C., Gubbins, D. & Alfè, D. Thermal and electrical conductivity of solid  
389 iron and iron-silicon mixtures at Earth's core conditions. *Earth Planet. Sci. Lett.* **393**, 159–  
390 164 (2014).

- 391 28. Ohta, K. e. a. Measurements of electrical and thermal conductivity of iron under Earth's core  
392 conditions **Abstract AGU Fall Meeting 2014** (2014).
- 393 29. Stacey, F. & Anderson, O. Electrical and thermal conductivities of Fe-Ni-Si alloy under core  
394 conditions. *Phys. Earth Planet. Int.* **124**, 153–162 (2001).
- 395 30. Stacey, F. & Loper, D. A revised estimate of the conductivity of iron alloy at high pressure  
396 and implications for the core energy balance. *Phys. Earth Planet. Int.* **161**, 13–18 (2007).
- 397 31. Zhang, P., Cohen, R. & Haule, K. Effects of electron correlations on transport properties of  
398 iron at Earth's core conditions. *Nature* **517**, 605–607 (2015).
- 399 32. Pourovskii, L., Mravlje, J., Ferrero, M., Parcollet, O. & Abrikosov, I. Impact of electronic  
400 correlations on the equation of state and transport in  $\epsilon$ -Fe. *Phys. Rev. B* **90**, 155120 (2014).
- 401 33. Masters, G. & Gubbins, D. On the resolution of density within the Earth. *Phys. Earth Planet.*  
402 *Int.* **140**, 159–167 (2003).
- 403 34. Cao, A. M. & Romanowicz, B. Constraints on density and shear velocity contrasts at the  
404 inner core boundary. *Geophys. J. Int.* **157**, 1146–1151 (2004).
- 405 35. Koper, K. D. & Dombrovskaya, M. Seismic properties of the inner core boundary from  
406 PKiKP/P amplitude ratios. *Earth Planet. Sci. Lett.* **237**, 680–694 (2005).
- 407 36. Tkalčić, H., Kennett, B. & Cormier, V. On the inner–outer core density contrast from  
408 PKiKP/PcP amplitude ratios and uncertainties caused by seismic noise. *Geophys. J. Int.*  
409 **179**, 425–443 (2009).

- 410 37. Souriau, A. Deep Earth structure – the Earth’s cores. In Schubert, G., Romanowicz, B. &  
411 Dziewonski, A. (eds.) *Treatise on geophysics*, vol. 1, chap. 19, 655–693 (Elsevier, Amster-  
412 dam, 2007).
- 413 38. Gubbins, D., Masters, G. & Nimmo, F. A thermochemical boundary layer at the base of  
414 Earth’s outer core and independent estimate of core heat flux. *Geophys. J. Int.* **174**, 1007–  
415 1018 (2008).
- 416 39. Alboussière, T., Deguen, R. & Melzani, M. Melting-induced stratification above the Earth’s  
417 inner core due to convective translation. *Nature* **466**, 744–747 (2010).
- 418 40. Dziewonski, A. & Anderson, D. Preliminary Reference Earth Model. *Phys. Earth Planet.*  
419 *Int.* **25**, 297–356 (1981).
- 420 41. Nomura, R. *et al.* Low core-mantle boundary temperature inferred from the solidus of pyro-  
421 lite. *Science* **343**, 522–524 (2014).
- 422 42. Tateno, S., Hirose, K., Komabayashi, T., Ozawa, H. & Ohishi, Y. The structure of Fe-Ni  
423 alloy in Earth’s inner core. *Geophys. Res. Lett.* **39**, L12305 (2012).
- 424 43. Martorell, B., Brodholt, J., Wood, I. G. & Vočadlo, L. The effect of nickel on the properties  
425 of iron at the conditions of the Earth’s inner core: *Ab initio* calculations of seismic wave  
426 velocities of Fe-Ni alloys. *Earth Planet. Sci. Lett.* **365**, 143–151 (2013).
- 427 44. Hirose, K., Labrosse, S. & Hernlund, J. Compositional state of Earth’s core. *Annual Review*  
428 *of Earth and Planetary Sciences* **41**, 657–691 (2013).

- 429 45. Morard, G., Andrault, D., Antonangeli, D. & Bouchet, J. Properties of iron alloys under the  
430 Earth's core conditions. *C. R. Geoscience* **346**, 130–139 (2014).
- 431 46. Badro, J., Côté, A. & Brodholt, J. A seismologically consistent compositional model of  
432 Earth's core. *Proc. Natl. Acad. Sci.* **111**, 7542–7545 (2014).
- 433 47. Jackson, J. *et al.* Melting of compressed iron by monitoring atomic dynamics. *Earth Planet.*  
434 *Sci. Lett.* **362**, 143–150 (2013).
- 435 48. Nguyen, J. & Holmes, N. Melting of iron at the physical conditions of the Earth's core.  
436 *Nature* **427**, 339–342 (2004).
- 437 49. Alfè, D., Gillan, M. & Price, G. *Ab initio* chemical potentials of solid and liquid solutions  
438 and the chemistry of the Earth's core. *J. Chem. Phys.* **116**, 7127–7136 (2002).
- 439 50. Belonoshko, A., Ahuja, R. & Johansson, B. Quasi-*ab Initio* molecular dynamic study of Fe  
440 melting. *Phys. Rev. Lett.* **84**, 3638–3641 (2000).
- 441 51. Laio, A., Bernard, S., Chiarotti, G. & Scandolo, E., S. Tosatti. Physics of iron at Earth's core  
442 conditions. *Science* **287**, 1027–1030 (2000).
- 443 52. Alfè, D., Gillan, M. & Price, G. Complementary approaches to the *ab initio* calculation of  
444 melting properties. *J. Chem. Phys.* **116**, 6170–6177 (2002).
- 445 53. Stacey, F. Thermodynamics of the Earth. *Rep. Prog. Phys.* **73**, 1–23 (2010).
- 446 54. Ichikawa, H., Tsuchiya, T. & Tange, Y. The P-V-T equation of state and thermodynamic  
447 properties of liquid iron. *J. Geophys. Res.* **119**, 240–252 (2014).



- 448 55. Gubbins, D., Alfe, D., Masters, G., Price, G. & Gillan, M. Can the Earth's dynamo run on  
449 heat alone? *Geophys. J. Int.* **155**, 609–622 (2003).
- 450 56. Stacey, F. Core properties, physical. In Gubbins, D. & Herrero-Bervera, E. (eds.) *Encyclo-*  
451 *pedia of Geomagnetism and Paleomagnetism*, 91–94 (Springer, 2007).
- 452 57. Ichikawa, H. & Tsuchiya, T. Atomic transport property of Fe-O liquid alloys in the Earth's  
453 outer core P,T condition. *Phys. Earth Planet. Int.* [dx.doi.org/10.1016/j.pepi.2015.03.006](https://doi.org/10.1016/j.pepi.2015.03.006)  
454 (2015).
- 455 58. Gubbins, D., Alfè, D., Masters, G., Price, G. & Gillan, M. Gross thermodynamics of two-  
456 component core convection. *Geophys. J. Int.* **157**, 1407–1414 (2004).
- 457 59. Davies, C. Cooling history of Earth's core with high thermal conductivity. *Phys. Earth*  
458 *Planet. Int.* [doi:10.1016/j.pepi.2015.03.007](https://doi.org/10.1016/j.pepi.2015.03.007) (2015).
- 459 60. Roberts, P. & King, E. On the genesis of the Earth's magnetism. *Rep. Prog. Phys.* **76**, 1–55  
460 (2013).
- 461 61. de Wijs, G. *et al.* The viscosity of liquid iron at the physical conditions of the Earth's core.  
462 *Nature* **392**, 805–807 (1998).
- 463 62. Lay, T., Hernlund, J. & Buffett, B. Core-mantle boundary heat flow. *Nat. Geosci.* **1**, 25–32  
464 (2009).
- 465 63. Nimmo, F. Energetics of the core. In Schubert, G. (ed.) *Treatise on Geophysics 2nd Edn*,  
466 *Vol. 9*, 31–65 (Elsevier, Amsterdam, 2014).

- 467 64. Jackson, A. & Livermore, P. On Ohmic heating in the Earth's core I: nutation constraints.  
468 *Geophys. J. Int.* **177**, 367–382 (2009).
- 469 65. Roberts, P., Jones, C. & Calderwood, A. Energy fluxes and ohmic dissipation in the Earth's  
470 core. In *Earth's core and lower mantle*, 100–129 (Contributions from the SEDI 2000, The  
471 7th Symposium, 2003).
- 472 66. Davies, J. & Davies, D. Earth's surface heat flux. *Solid Earth* **1**, 5–24 (2010).
- 473 67. Andrault, D. *et al.* Solidus and liquidus profiles of chondritic mantle: Implication for melting  
474 of the Earth across its history. *Earth Planet. Sci. Lett.* **304**, 251–259 (2011).
- 475 68. Nakagawa, T. & Tackley, P. Influence of combined primordial layering and recycled MORB  
476 on the coupled thermal evolution of Earth's mantle and core. *Geochem. Geophys. Geosys.*  
477 **15**, 619–633 (2014).
- 478 69. Driscoll, P. & Bercovici, D. On the thermal and magnetic histories of Earth and Venus:  
479 Influences of melting, radioactivity, and conductivity. *Phys. Earth Planet. Int.* **236**, 36–51  
480 (2014).
- 481 70. Labrosse, S. Thermal and compositional stratification of the inner core. *C. R. Geosci.* **346**,  
482 119–129 (2014).
- 483 71. Kennett, B., Engdahl, E. & Buland, R. Constraints on seismic velocities in the Earth from  
484 traveltimes. *Geophys. J. Int.* **122**, 108–124 (1995).

- 485 72. Braginsky, S. Dynamics of the stably stratified ocean at the top of the core. *Phys. Earth*  
486 *Planet. Int.* **111**, 21–34 (1999).
- 487 73. Loper, D. Some thermal consequences of a gravitationally powered dynamo. *J. Geophys.*  
488 *Res.* **831**, 5961–5970 (1978).
- 489 74. Helffrich, G. & Kaneshima, S. Causes and consequences of outer core stratification. *Phys.*  
490 *Earth Planet. Int.* **223**, 2–7 (2013).
- 491 75. Buffett, B. & Seagle, C. Stratification of the top of the core due to chemical interactions with  
492 the mantle. *J. Geophys. Res.* **115**, B04407 (2010).
- 493 76. Gubbins, D. & Davies, C. The stratified layer at the core-mantle boundary caused by barod-  
494 iffusion of Oxygen, Sulphur and Silicon. *Phys. Earth Planet. Int.* **215**, 21–28 (2013).
- 495 77. Moffatt, H. & Loper, D. The magnetostrophic rise of a buoyant parcel in the Earth’s core.  
496 *Geophys. J. Int.* **117**, 394–402 (1994).
- 497 78. Buffett, B. Geomagnetic fluctuations reveal stable stratification at the top of the Earth’s core.  
498 *Nature* **507**, 484–487 (2014).
- 499 79. Helffrich, G. & Kaneshima, S. Outer-core compositional stratification from observed core  
500 wave speed profiles. *Nature* **468**, 807–809 (2010).
- 501 80. Labrosse, S. Thermal evolution of the core with a high thermal conductivity. *Phys. Earth*  
502 *Planet. Int.* doi:10.1016/j.pepi.2015.02.002 (2015).

- 503 81. Gubbins, D., Alfè, D., Davies, C. & Pozzo, M. On core convection and the geo-  
504 dynamo: Effects of high electrical and thermal conductivity. *Phys. Earth Planet. Int.*  
505 doi:10.1016/j.pepi.2015.04.002 (2015).
- 506 82. Nakagawa, T. & Tackley, P. Lateral variations in CMB heat flux and deep mantle seismic  
507 velocity caused by a thermal-chemical-phase boundary layer in 3D spherical convection.  
508 *Earth Planet. Sci. Lett.* **271**, 348–358 (2007).
- 509 83. Olson, P. & Christensen, U. The time-averaged magnetic field in numerical dynamos with  
510 non-uniform boundary heat flow. *Geophys. J. Int.* **151**, 809–823 (2002).
- 511 84. Aubert, J., Amit, H., Hulot, G. & Olson, P. Thermochemical flows couple the Earth's inner  
512 core growth to mantle heterogeneity,. *Nature* **454**, 758–761 (2008).
- 513 85. Gibbons, S. & Gubbins, D. Convection in the Earth's core driven by lateral variations in  
514 core-mantle boundary heat flux. *Geophys. J. Int.* **142**, 631–642 (2000).
- 515 86. Hollerbach, R. & Jones, C. Influence of the Earth's inner core on geomagnetic fluctuations  
516 and reversals. *Nature* **365**, 541–543 (1993).
- 517 87. Deguen, R. Structure and dynamics of Earth's inner core. *Earth Planet. Sci. Lett.* **333–334**,  
518 211–225 (2012).
- 519 88. Lasbleis, M. & Deguen, R. Building a regime diagram for Earth's inner core. *Phys. Earth*  
520 *Planet. Int.* doi:10.1016/j.pepi.2015.02.001 (2015).

- 521 89. Korenaga, J. Urey ratio and the structure and evolution of Earth's mantle. *Rev. Geophys.* **46**,  
522 2007RG000241 (2008).
- 523 90. Lythgoe, K., Rudge, J., Neufeld, J. & Deuss, A. The feasibility of thermal and compositional  
524 convection in Earth's inner core. *Geophys. J. Int.* **385**, 764–782 (2015).
- 525 91. Monnereau, M., Calvet, M., Margerin, L. & Souriau, A. Lopsided growth of Earth's inner  
526 core. *Science* **328**, 1014–1017 (2010).
- 527 92. Aubert, J., Finlay, C. & Fournier, A. Bottom-up control of geomagnetic secular variation by  
528 the Earth's inner core. *Nature* **502**, 219–223 (2013).
- 529 93. Olson, P. & Deguen, R. Eccentricity of the geomagnetic dipole caused by lopsided inner core  
530 growth. *Nat. Geosci.* **5**, 565–569 (2012).
- 531 94. Nakagawa, T. & Tackley, P. Implications of high core thermal conductivity on Earth's coupled  
532 mantle and core evolution. *Geophys. Res. Lett.* **40**, 1–5 (2013).
- 533 95. Labrosse, S., Hernlund, J. & Coltice, N. A crystallizing dense magma ocean at the base of  
534 the Earth's mantle. *Nature* **450**, 866–869 (2007).
- 535 96. Ziegler, L. B. & Stegman, D. R. Implications of a long-lived basal magma ocean in generating  
536 Earth's ancient magnetic field. *Geochem. Geophys. Geosys.* **14**, 4735–4742 (2013).
- 537 97. Stevenson, D. How to keep a dynamo running in spite of high thermal conductivity **Abstract**  
538 **AGU Fall Meeting 2012** (2012).

- 539 98. Amit, H. Can downwelling at the top of the Earth's core be detected in the geomagnetic  
540 secular variation? *Phys. Earth Planet. Int.* **229**, 110–121 (2014).
- 541 99. Lesur, V., Whaler, K. & Wardinski, I. Are geomagnetic data consistent with stably stratified  
542 flow at the core-mantle boundary? *Geophys. J. Int.* 929–946 (2015).
- 543 100. Buffet, B., & Matsui, H. A power spectrum for the geomagnetic dipole moment. *Earth*  
544 *Planet. Sci. Lett.* **411**, 20–26 (2015).

545 **Supplementary Information** is linked to the online version of the paper at [www.nature.com/nature](http://www.nature.com/nature).

546 **Acknowledgements** CD is supported by Natural Environment Research Council (NERC) fellowships  
547 NE/H01571X/1 and NE/L011328/1 and a Green Scholarship at IGPP. DG is supported by NSF Grant EAR/  
548 1065597 and NERC Grant NE/I012052/. MP is supported by NERC grant NE/H02462X/1 and NERC grant  
549 NE/M000990/1 to DA.

550 **Author Information** Reprints and permissions information is available at [www.nature.com/reprints](http://www.nature.com/reprints). The  
551 authors declare that they have no competing financial interests. Correspondence and requests for materials  
552 should be addressed to Chris Davies. (email: [c.davies@leeds.ac.uk](mailto:c.davies@leeds.ac.uk)).

Symbol	100%Fe	82%Fe-8%O-10%Si	79%Fe-13%O-8%Si	81%Fe-17%O-2%Si
$\Delta\rho$ (gm/cc)	0.24 [17]	0.6 [40]	0.8 [33]	1.0 [33]
$c_O^S$	–	0.0002 [14]	0.0004 [14]	0.0006 [81]
$c_{Si}^S$	–	0.0554 [14]	0.0430 [14]	0.0096 [81]
$c_O^L$	–	0.0256 [14]	0.0428 [14]	0.0559 [81]
$c_{Si}^L$	–	0.0560 [14]	0.0461 [14]	0.0115 [81]
$C_p$ (J/kg/K)	715 [55] — 800 [53]	–	–	–
$\gamma$	1.4 [56] — 1.5 [17, 55]	–	–	–
$\Delta S(r_i)$ ( $k_B$ )	1.05 [17]	–	–	–
$L(r_i)$ (MJ/kg)	0.75	–	–	–
$T_m(r_i)$ (K)	6350 [17, 20]	5900	5580	5320
$\left. \frac{dT_m}{dP} \right _{r_i}$ (K/GPa)	9.01	9.01	9.01	9.01
$\alpha_T(r_i)$ ( $\times 10^{-5}/K$ )	1.0 [54, 55]	–	–	–
$T_a(r_o)$ (K)	4735 [17, 20]	4290	4105	3910
$\left. \frac{\partial T_a}{\partial P} \right _{r_i}$ (K/GPa)	6.96	6.25	6.01	5.81
$\left. \frac{\partial T_a}{\partial r} \right _{r_o}$ (K/km)	-1.15	-1.03	-1.00	-0.96
$\sigma$ ( $\times 10^6$ S/m)	1.36 [25], 1.4 [23], 1.86 [26,*]	1.12 [25]	1.11 [25]	1.18 [25]
$k$ (W/m/K)	159 [25], 150 [23], 170 [26]	107 [25]	99 [25]	101 [25]
$D_O$ ( $\times 10^{-8}$ m <sup>2</sup> /s)[25]	–	1.31	1.30	–
$D_{Si}$ ( $\times 10^{-8}$ m <sup>2</sup> /s)[25]	–	0.52	0.46	–
$\nu$ [25]	6.9	6.8	6.7	–
$\alpha_O^D$ ( $\times 10^{-12}$ kg/m <sup>3</sup> s)	–	0.72	0.97	1.11
$\alpha_{Si}^D$ ( $\times 10^{-12}$ kg/m <sup>3</sup> s)	–	1.19	1.10	40.6
		O	Si	
$\alpha_c$ [46, 49]	–	1.1	0.87	
$\left( \frac{\partial \mu}{\partial c_X} \right)_{P,T}$ (ev/atom)	–	$1.02 \times 10^{10}$	$1.40 \times 10^{10}$	

**Table 1: Core material properties for pure iron and three Fe-O-Si mixtures.** Models are named after the mass concentrations of mixtures of Fe, O, and Si corresponding to the given density jump. Quantities in the first section define the core chemistry model used in this review. Numbers in the second section determine the core temperature properties given in the third section. The core temperature is assumed to follow an adiabat, denoted  $T_a$ , and the melting temperature of the core alloy is denoted  $T_m$ . CMB values for transport properties calculated along the corresponding adiabats are given in section four. The CMB radius is denoted  $r_o = 3480$  km, the present-day ICB radius is  $r_i = 1221$  km and  $k_B$  is Boltzmann's constant. Where a range is given, numbers highlighted in red are used in the core models in section 3. \*: This value was derived at a presumed CMB temperature of 3750 K.

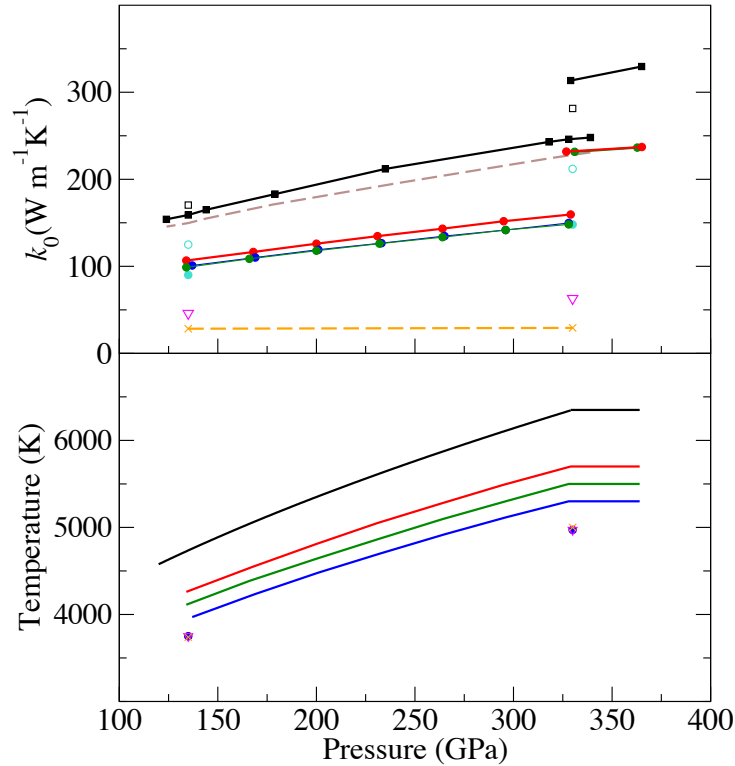


Figure 1: **Comparison of thermal conductivity estimates (top) and adiabatic temperature profiles (bottom) from different studies.** The core chemistry models in Table 1 are shown in black (100%Fe)<sup>24</sup>, red (82%Fe-8%O-10%Si)<sup>25</sup>, green (79%Fe-13%O-8%Si)<sup>25</sup> and blue (81%Fe-17%O-2%Si)<sup>81</sup>. Data from two other recent studies are shown for pure Fe (open black squares<sup>26</sup>, brown line<sup>23</sup> using the volume-temperature data of Pozzo et al 2012<sup>24</sup>), a mixture of 76.8%Fe-23.2%O (open blue circles<sup>26</sup>) and a mixture of 77.5%Fe-22.5%Si (filled blue circles<sup>26</sup>). Two older estimates of  $k$  are shown by the open magenta triangles<sup>29</sup> and orange crosses<sup>30</sup>. Inner core values were obtained from calculations on solid mixtures<sup>27</sup>.



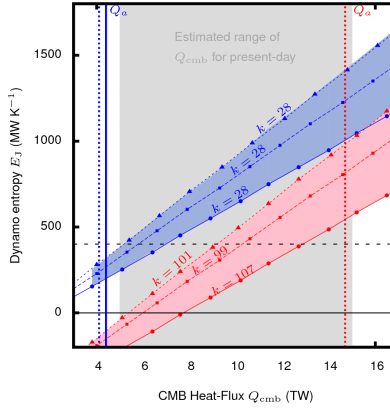


Figure 2: **Present-day core energy budget.** Models shown in red use recent estimates of the thermal conductivity  $k$  (red in Figure 1) calculated for ICB density jumps  $\Delta\rho = 0.6$  (solid line), 0.8 (long-dashed line) and 1.0 gm/cc (short-dashed line); models in blue all use an old value<sup>30</sup>  $k = 28 \text{ W m}^{-1} \text{ K}^{-1}$ . Other parameters are given in Table 1. Thick dashed lines indicate ranges for the heat  $Q_a$  lost down the core adiabat. The black dotted line indicates a plausible estimate<sup>65</sup> for  $E_J$ . Dynamo action requires  $E_J > 0$ . The grey shaded region indicates present-day estimates of CMB heat flow<sup>62,63</sup>. For  $Q_{\text{cmb}} < Q_a$  any convection in the uppermost core is driven compositionally against thermal stratification.

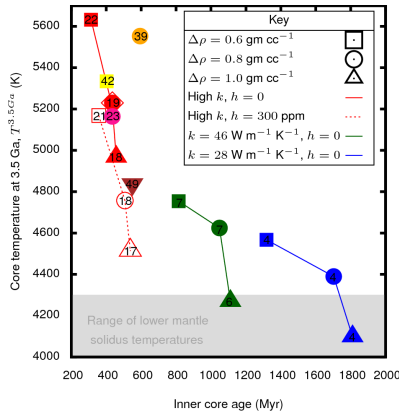


Figure 3: **Core thermal evolution.** Numbers inside each symbol give CMB heat flow (TW) at 3.5 Ga. High  $k$  models use the red profiles in Figure 1 that have been calculated for each  $\Delta\rho$ ; models in blue and green use the same  $k$  for each  $\Delta\rho$ . Models joined by lines use  $E_J = 0$  prior to inner core formation, after which  $Q_{cmb}$  is set constant to ensure the outer core remains just superadiabatic. Results from other recent studies are shown in yellow<sup>68</sup>, pink<sup>63</sup>, orange<sup>80</sup> and maroon<sup>69</sup>. The inverted triangle denotes that  $\Delta\rho$  did not enter into this formulation. Open diamond denotes the reference case in Figure 4.

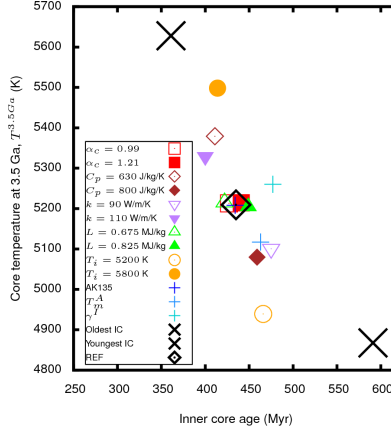


Figure 4: **Dependence of core thermal history predictions on various material properties.**

Each model uses identical parameters to the reference model, denoted REF and shown with a red diamond in Figure 3, except the quantity referred to in the legend. A  $\pm 10\%$  variation in  $\alpha_c$ ,  $C_p$  and  $L$  from the values in Table 1 has been assumed. Values of  $k$  refer to the CMB and span the range in Table 1. Values of  $T_i$  span the  $\pm 300$  K error estimates<sup>14,20</sup> described in the text. AK135 is a model of core density<sup>71</sup>.  $T_m^A$  is a recent experimentally-determined melting curve<sup>20</sup>. Model  $\gamma^I$  uses depth-dependent  $\gamma$  taken from a recent study<sup>54</sup>. Crosses show the youngest and oldest inner core ages that can be achieved by combining the other variations.